

# PEaRL: Pathway-Enhanced Representation Learning for Gene and Pathway Expression Prediction from Histology

Sejuti Majumder<sup>1</sup>, Saarthak Kapse<sup>1</sup>, Moinak Bhattacharya<sup>1</sup>, Xuan Xu<sup>2</sup>,  
Alisa Yurovsky<sup>1</sup>, Prateek Prasanna<sup>1</sup>

<sup>1</sup>Department of Biomedical Informatics, Stony Brook University, NY, USA,

<sup>2</sup>Department of Computer Science, Stony Brook University, NY, USA

sejuti.majumder@stonybrook.edu, saarthak.kapse@stonybrook.edu, xuaxu@cs.stonybrook.edu,  
moinak.bhattacharya@stonybrook.edu, alisa.yurovsky@stonybrookmedicine.edu,  
prateek.prasanna@stonybrook.edu

## Abstract

*Integrating histopathology with spatial transcriptomics (ST) provides a powerful opportunity to link tissue morphology with molecular function. Yet most existing multimodal approaches rely on a small set of highly variable genes, which limits predictive scope and overlooks the coordinated biological programs that shape tissue phenotypes. We present **PEaRL** (Pathway Enhanced Representation Learning), a multimodal framework that represents transcriptomics through pathway activation scores computed with ssGSEA. By encoding biologically coherent pathway signals with a transformer and aligning them with histology features via contrastive learning, PEaRL reduces dimensionality, improves interpretability, and strengthens cross-modal correspondence. Across three cancer ST datasets—breast, skin, and lymph node—PEaRL consistently outperforms SOTA methods, yielding higher accuracy for both gene- and pathway-level expression prediction (up to 58.9% and 20.4% increase in Pearson correlation coefficient compared to SOTA). These results demonstrate that grounding transcriptomic representation in pathways produces more biologically faithful and interpretable multimodal models, advancing computational pathology beyond gene-level embeddings.*

## 1. Introduction

Recent advancements in digital pathology have led to improvements in cell and tissue-level classification [9, 12, 28, 41], survival prediction [5, 45], and automated diagnostics [33]. Deep networks have demonstrated impressive capabilities in identifying phenotypic patterns associated with disease progression. However, despite these improve-

ments, a fundamental challenge remains, clinical outcomes and disease states are typically determined by more than just morphological patterns. Tumor microenvironments are inherently complex, and direct correlations between tissue phenotype and molecular function remain elusive. This limitation motivates the need for approaches that integrate histopathology with molecular data to provide a more comprehensive view of disease mechanisms.

Transcriptomics [16, 30] enables the genome-wide quantification of gene expression, providing insights into the molecular mechanisms underlying various biological processes. Advances in single-cell RNA sequencing [38, 39] have allowed for high-resolution profiling of gene expression at the individual cell level, improving the classification of distinct cell types and states. However, traditional bulk transcriptomics and single-cell sequencing approaches suffer from significant limitations. Bulk RNA sequencing averages gene expression across a heterogeneous population of cells, obscuring cell-specific expression patterns. Meanwhile, single-cell approaches, despite their high resolution, require tissue dissociation, leading to the loss of crucial spatial information necessary for understanding tissue organization and cell-cell interactions.

Spatial transcriptomics (ST) bridges the gap between transcriptomics and histology by preserving the spatial context of gene expression within intact tissue sections [34, 35]. Unlike bulk and single-cell RNA sequencing, ST enables the measurement of gene expression at precise tissue locations, facilitating the study of cell states and molecular interactions in their native microenvironments. This integration of spatial information with transcriptomic data makes ST ideal for multimodal learning with histopathology images. By aligning morphological patterns with spatially resolved gene expression, ST provides a unique opportunity to uncover the functional underpinnings of histopathologi-

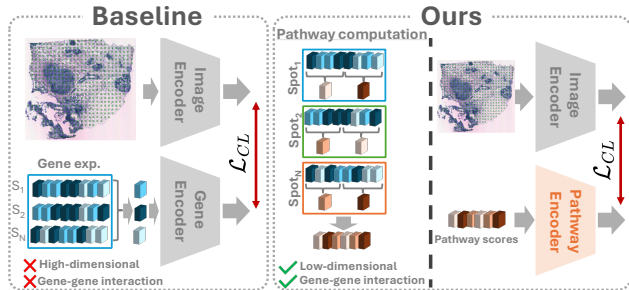


Figure 1. **Multimodal Learning with PEaRL.** PEaRL considers gene-gene interactions via pathways which not only addresses the curse of high gene dimensionality but also acts as a molecular driver of tissue morphology leading to biologically meaningful representation learning between images and molecular data. We employ PEaRL for both gene and pathway expression prediction and also show its utility in survival analysis.

cal changes, ultimately improving disease diagnosis, prognosis, and therapeutic targeting.

Several computational methods have been developed to integrate histopathology images with transcriptomic data, yet this task remains fundamentally challenging. For the task of gene expression prediction from histology images, the overlapping but distinct information captured by these two modalities make the perfect reconstruction of transcriptomics profiles from morphology infeasible. Additionally, gene expression is both high-dimensional (often 15,000+ genes) and sparse, creating the curse of dimensionality that complicates model training. Early approaches such as STNet [10], HisToGene [31], His2ST [50], and THItToGene [19] demonstrated the feasibility of mapping histology patches to gene expression using convolutional networks, transformers, or graph neural networks. However, these methods typically focused on predicting a small subset of highly variable or marker genes, which limited their predictive scope and often failed to capture the broader heterogeneity of transcriptomic signals. To overcome these constraints, more recent work has explored contrastive learning, which aligns histology and gene expression features in a shared latent space rather than directly regressing expression values. By encouraging embeddings from the same spatial location to cluster together, contrastive learning provides a more flexible way to capture cross-modal correspondences while reducing sensitivity to sparsity and noise in ST data. Methods such as HisToGene [31], BLEEP [46], and mclSTExp [29] highlight this trend, showing that contrastive objectives can improve alignment between image and transcriptomics and support more generalizable multimodal representations.

While gene-level encoding has been common practice in existing multimodal ST methods, it suffers from both technical and biological limitations. Using a small set of highly

variable genes to mitigate high dimensionality limits both predictive scope and fails to capture the coordinated molecular programs that drive tissue morphology. Meanwhile, pathways, defined as sets of genes with known interactions and shared cellular functions, aggregate signals across all expressed genes into compact, biologically coherent modules. For example, genes such as the *HLA-A*, *HLA-B*, and *STAT1* may individually appear as highly variable and be used as markers of immune activity. However, considered in isolation, they do not reflect the broader immune processes at play. When examined together as part of the Hallmark Allograft Rejection pathway, these genes capture coordinated immune responses involving antigen presentation and interferon signaling, which more coherently explain the widespread lymphocyte infiltration observed in histology. Pathways provide a natural solution to these challenges. Compared to raw gene-level vectors, pathway scores reduce dimensionality while preserving the functional underpinnings of tissue organization and disease progression. Furthermore, because pathways represent interpretable biological processes, they constitute semantically meaningful tokens that can align more naturally with histological patterns, for instance, immune infiltration in histology corresponding to the activation of interferon or T-cell signaling pathways (see Fig. 1).

**Our approach.** We introduce **PEaRL (Pathway Enhanced Representation Learning)**, a multimodal framework that leverages pathway activation scores, computed via single-sample gene set enrichment analysis (ssGSEA), as the transcriptomic input. Instead of relying on individual genes, PEaRL encodes biologically coherent pathway signals using a transformer-based pathway encoder, while histology features are extracted with an image encoder. A contrastive objective aligns these two modalities in a shared latent space, enabling robust cross-modal correspondence. We evaluate PEaRL on three spatial transcriptomics oncology datasets, breast [2], skin [18], and lymph node [27], and demonstrate improved performance in both gene- and pathway-level expression prediction compared to existing methods. By grounding transcriptomic representation in pathways, PEaRL reduces dimensionality, enhances interpretability, and achieves more biologically faithful multimodal alignment.

Our contributions are threefold:

- We propose a pathway-based representation of spatial transcriptomics data, enabling biologically enriched embeddings for multimodal learning.
- We design a multimodal framework that combines a transformer pathway encoder, an image encoder, and contrastive learning to jointly predict both pathway and gene expression from histology.
- Through extensive experiments on multiple cancer datasets, we show that PEaRL consistently outperforms

prior approaches in expression prediction and further demonstrates utility in downstream survival analysis.

## 2. Related Work

### 2.1. Spatial Gene Expression Prediction

Spatial transcriptomics (ST) has motivated a growing body of work on predicting gene expression directly from histology images. Early approaches such as STNet [10] leveraged CNN-derived features from H&E patches to predict expression of a fixed gene panel, demonstrating the feasibility of image-to-transcriptome prediction. HisToGene [31] extended this idea with a Vision Transformer jointly encoding histology and spatial coordinates, enabling higher-resolution predictions. Hist2ST [50] further decomposed the task into local, global, and neighborhood modules via ConvMixer, Transformer, and GraphSAGE. More recently, hybrid architectures such as THItToGene [19] integrated multi-scale convolutional and attention-based blocks to better capture tumor microenvironmental cues.

Despite these advances, most regression-based models still rely on highly variable or marker genes, limiting predictive scope and failing to capture broader transcriptomic heterogeneity. To overcome these challenges, contrastive frameworks have been introduced. BLEEP [46] aligned histology and gene expression embeddings through a CLIP-style objective, imputing expression with k-nearest neighbors. MCLSTExp [29] unified histology, expression, and spatial coordinates into a single contrastive learning framework, modeling spots as “words” and tissue regions as “sentences.” These methods highlight the promise of contrastive objectives for robust multimodal alignment.

### 2.2. Pathway-Based Representations

Meanwhile, pathway-level representations have been increasingly explored in survival prediction as a way to overcome the high dimensionality and noise of gene-level features. By aggregating genes into functional modules, pathway scores provide compact and interpretable signals that link molecular programs to prognosis. For example, SurvPath [15] models dense interactions between pathways and histology patches using a multimodal transformer, improving patient risk stratification. Cox-Path [25] integrates multi-omics data into a pathway-informed graph convolutional network, capturing pathway–pathway interactions before Cox regression. More recently, PIBD [52] addresses redundancy in multimodal survival prediction by disentangling common and modality-specific features across pathways and images. Beyond general frameworks, disease-specific studies such as PPAR-related prognostic modeling in hepatocellular carcinoma (HCC) [20] further demonstrate how pathway activity can define subgroups with distinct outcomes and therapeutic responses. Together, these

works highlight pathways as natural semantic units for survival analysis and motivate their use in multimodal frameworks like PEaRL.

### 2.3. Histopathology Representation Learning

Parallel to ST-specific efforts, the field of histopathology has witnessed rapid progress in image representation learning. Weakly supervised whole-slide image (WSI) analysis has been the dominant paradigm, with multiple instance learning (MIL) frameworks widely applied to tasks such as cancer classification [37, 49] and survival prediction [5, 45]. With the rise of self-supervised learning (SSL), approaches such as SimCLR, MoCo, and DINO have been adapted to WSIs, giving rise to pathology foundation models like CTransPath [42], HIPT [6], and UNI [7], which generalize across diverse downstream tasks.

In the multimodal domain, CLIP [32] inspired vision–language pretraining has been adapted to pathology through PLIP [13], CONCH [24], and Prov-GigaPath [47], which align histology images with captions or molecular data. These models have established new benchmarks in retrieval, classification, and subtyping, highlighting the utility of large-scale multimodal pretraining. Importantly, the availability of ST data has opened opportunities for aligning histology with molecular profiles at spatial resolution, motivating specialized frameworks such as BLEEP and mclSTExp that explicitly target expression prediction.

## 3. Methods

**Overview.** PEaRL employs multimodal learning to integrate histological image features with ST data for gene and pathway expression prediction (Fig. 2). The training framework consists of two key components: the *pathway encoder* and the *vision encoder*, which generate embeddings for pathways and histological images, respectively. These embeddings are aligned using contrastive learning to establish meaningful cross-modal representations.

### 3.1. Pathway Encoder

The pathway encoder integrates biological context by leveraging pathway scores derived from gene expression. A biological pathway can be defined as a network of molecular interactions [21] where genes ( $G$ ) function together in a coordinated manner to drive cellular processes such as metabolism, signaling, and regulation that, in turn, influence the cellular structure and tissue organization.

To compute pathway scores, we apply single-sample Gene Set Enrichment Analysis (ssGSEA) [1] directly on the expression matrix. Unlike GSEA [36], which compares gene expression between two predefined groups (e.g., diseased vs. healthy samples) to determine pathway enrichment at a population level, ssGSEA computes an enrichment score for each sample independently by ranking genes

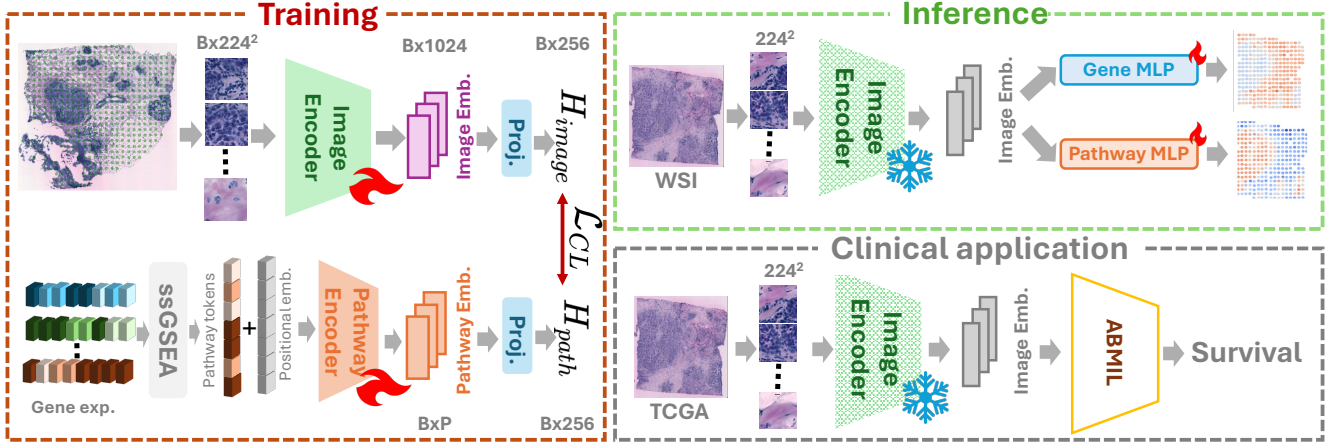


Figure 2. Overview of PEaRL framework. The framework begins with extracting patches corresponding to spatial transcriptomics spots and feeding them to the image encoder to get image embeddings. We compute the pathway scores from the high dimensional gene expression data corresponding to the spatial transcriptomics spots and feed it as an input to the transformer based pathway encoder along with the positional embeddings. The image embeddings and pathway embeddings are aligned via contrastive learning. The learned image embeddings are then used for downstream gene and pathway expression prediction.

and summing their weighted expression values. This enables pathway activity assessment at a spot level, capturing spatial heterogeneity across tissue sections. Given a pathway  $P_i$  containing  $G_{P_i}$  genes, where  $P$  denotes the number of pathways considered, the Normalized Enrichment Score (NES) for a spot  $s$  is computed as:

$$NES_s(P_i) = \frac{ES_s(P_i)}{\mathbb{E}[|ES_s(P_{\text{null}})|]} \quad (1)$$

where  $ES_s(P_i)$  is the enrichment score of pathway  $P_i$  in spot  $s$ , computed from the ranked gene expression profile of that spot;  $P_{\text{null}}$  are random gene sets of the same size as  $P_i$ ; and the denominator normalizes by the expected score from these null sets. Thus,  $NES_s(P_i)$  serves as the pathway score for pathway  $P_i$  in spot  $s$ .

Thus, for each point  $s$ , we compute a pathway score vector  $x_s$ . The dimensionality of this vector corresponds to the number of pathways included for a given dataset:

$$x_s \in \mathbb{R}^P \quad (2)$$

**Transformer as the pathway encoder.** For a batch of  $N$  spots, let  $X \in \mathbb{R}^{N \times P}$  denote the ssGSEA pathway score matrix. We encode spatial position using globally normalized coordinates such that it maps the coordinates of the spots across the dataset to a common reference point. This global normalization ensures that a batch of  $N$  spots can contain positions from different slides while remaining comparable in a shared coordinate space. For raw spot coordinates  $C \in \mathbb{R}^{N \times 2}$  ( $x, y$ ), we compute:

$$\tilde{C} = \frac{C - \mu}{\sigma} \quad (3)$$

with mean  $\mu \in \mathbb{R}^2$  and standard deviation  $\sigma \in \mathbb{R}^2$  estimated over all spots in the split (train or validation). A learnable positional encoder  $\phi : \mathbb{R}^2 \rightarrow \mathbb{R}^P$  (implemented as a MLP) maps  $\tilde{C}$  to  $\phi(\tilde{C}) \in \mathbb{R}^{N \times P}$ . The transformer input is the sum:

$$H_0 = X + \phi(\tilde{C}) \in \mathbb{R}^{N \times P} \quad (4)$$

We use a two-layer Transformer encoder with standard multi-head self-attention (MHSA). For each head  $h$ ,

$$Q_h = H_0 W_Q^{(h)}, \quad K_h = H_0 W_K^{(h)}, \quad V_h = H_0 W_V^{(h)} \quad (5)$$

and attention is computed as

$$\text{Attn}_h(H_0) = \text{softmax}\left(\frac{Q_h K_h^\top}{\sqrt{d_k}}\right) V_h \quad (6)$$

where  $W_Q^{(h)}, W_K^{(h)}, W_V^{(h)} \in \mathbb{R}^{P \times d_k}$  and  $d_k$  is the per-head key/query dimension. Outputs from all heads are concatenated and projected, followed by a position-wise feed-forward network with residual connections and layer normalization. The encoder output:

$$Z \in \mathbb{R}^{N \times P} \quad (7)$$

provides pathway embeddings that integrate pathway activity with spatial context.

After obtaining the output from transformer, we apply a projection head to map each spot's pathway embedding into a 256-dimensional space for multimodal alignment and contrastive learning:

$$H_{\text{path}} = \text{MLP}(Z) \in \mathbb{R}^{N \times 256} \quad (8)$$

### 3.2. Vision Encoder

To extract histological features, we employ UNI v1 [7], a pre-trained foundational model trained on 100k whole slide images, making it an ideal choice for encoding rich morphological features from H&E stained tissue sections. To process histopathology images, we first extract  $224 \times 224$  patches from whole slide images, ensuring that each patch corresponds to a ST spot. Each patch  $I_i$  in the batch of  $N$  spots/patches is passed through the UNI encoder to obtain a 1024 dimensional image embedding. Since our spot embeddings are 256 dimensional, we apply projection head to align the image feature dimension with the spot embedding space. Additionally we fine-tune the last 4 layers of UNI, allowing the model to adapt to this domain.

$$Z_{\text{image}} = \text{UNI}(I) \in \mathbb{R}^{N \times 1024} \quad (9)$$

$$H_{\text{image}} = \text{MLP}(Z_{\text{image}}) \in \mathbb{R}^{N \times 256} \quad (10)$$

### 3.3. Training and Inference

**Stage 1: Contrastive pretraining.** We learn a shared 256-dimensional space by aligning image and pathway embeddings with a symmetric contrastive loss. The  $H_{\text{image}} \in \mathbb{R}^{N \times 256}$  and  $H_{\text{path}} \in \mathbb{R}^{N \times 256}$  are then L2-normalized for a batch of  $N$  matched image–pathway pairs, followed by computing similarity logits as follows:

$$\mathbf{S} = \frac{H_{\text{image}} H_{\text{path}}^\top}{\tau} \in \mathbb{R}^{N \times N}, \quad (11)$$

where  $\tau > 0$  is a learnable temperature. With identity targets (treating diagonal elements as positives for contrastive learning), we optimize row-wise and column-wise cross-entropy (CE):

$$\mathcal{L}_{\text{img} \rightarrow \text{path}} = \frac{1}{N} \sum_{i=1}^N \text{CE}(\text{softmax}(\mathbf{S}_{i,:}), i), \quad (12)$$

$$\mathcal{L}_{\text{path} \rightarrow \text{img}} = \frac{1}{N} \sum_{j=1}^N \text{CE}(\text{softmax}(\mathbf{S}_{:,j}), j). \quad (13)$$

The symmetric contrastive objective is

$$\mathcal{L}_{\text{CL}} = \frac{1}{2} (\mathcal{L}_{\text{img} \rightarrow \text{path}} + \mathcal{L}_{\text{path} \rightarrow \text{img}}). \quad (14)$$

### Stage 2: Supervised prediction heads (frozen backbone).

After contrastive pretraining, we freeze the backbone and train two lightweight MLP heads ( $f_{\text{path}}$  and  $f_{\text{gene}}$ ) on top of the image embeddings. For a batch, let  $H_{\text{image}} \in \mathbb{R}^{N \times 256}$  denote these embeddings. We predict pathway scores and gene expression with two heads as follows:

$$\hat{y}_{\text{path}} = f_{\text{path}}(H_{\text{image}}) \in \mathbb{R}^{N \times P}, \quad (15)$$

$$\hat{y}_{\text{gene}} = f_{\text{gene}}(H_{\text{image}}) \in \mathbb{R}^{N \times g}, \quad (16)$$

where  $g$  denotes the number of highly variable genes (HVGs). We train these heads with mean-squared error (MSE) against ground truth pathway scores  $y_{\text{path}} \in \mathbb{R}^{N \times P}$  and gene expression  $y_{\text{gene}} \in \mathbb{R}^{N \times g}$ :

$$\mathcal{L}_{\text{path}} = \frac{1}{N \cdot P} \|\hat{y}_{\text{path}} - y_{\text{path}}\|_2^2, \quad (17)$$

$$\mathcal{L}_{\text{gene}} = \frac{1}{N \cdot g} \|\hat{y}_{\text{gene}} - y_{\text{gene}}\|_2^2. \quad (18)$$

The supervised objective for head training is the sum:

$$\mathcal{L}_{\text{sup}} = \mathcal{L}_{\text{path}} + \mathcal{L}_{\text{gene}}, \quad (19)$$

**Inference.** At test time, an input patch  $I_{\text{test}}$  is passed through the trained image encoder and projection head to obtain  $h_{\text{image}}^{\text{test}} \in \mathbb{R}^{256}$ . The pathway and gene predictions are then produced directly by the trained MLP heads:

$$\hat{y}_{\text{path}}^{\text{test}} = f_{\text{path}}(h_{\text{image}}^{\text{test}}), \quad (20)$$

$$\hat{y}_{\text{gene}}^{\text{test}} = f_{\text{gene}}(h_{\text{image}}^{\text{test}}). \quad (21)$$

## 4. Experiments and Results

We evaluate PEaRL on gene expression and pathway expression, along with survival analysis as a downstream task.

### 4.1. Dataset and Implementation

**Datasets.** We evaluate PEaRL using three cancer-focused spatial transcriptomics datasets curated from the HEST-1k Library [17], a standardized multimodal resource of paired histology and gene expression profiles. The breast cancer dataset [2] comprises 36 tissue sections with 13,620 spatial spots. The skin cancer dataset [18] contains 12 samples with 8,671 spots, while the lymph cancer dataset [27] consists of 24 samples with 74,220 spots.

**Data preprocessing and pathway annotation.** We first filtered out genes detected in fewer than 1,000 spots, followed by total-count normalization to 10,000 counts per spot and logarithmic transformation. We applied 8-neighbor smoothing to reduce spot-level noise like high sparsity while preserving local spatial continuity in tissue structure. Highly variable genes (HVGs) were then selected using Scanpy [44], retaining the top 1,000 HVGs ( $g$ ) for each dataset. For pathway annotation, we integrated gene sets from Reactome [8] and MSigDB [23], and quantified pathway activity at the single-spot level using single-sample gene set enrichment analysis (ssGSEA) [1]. This yielded  $P = 775$  pathways for the breast cancer dataset,  $P = 1,100$  pathways for the lymph dataset, and  $P = 609$  pathways for the skin dataset.

Table 1. Performance comparison on **Gene Expression** prediction across datasets. Results are mean  $\pm$  std. Best per column in **bold**.

Method	Breast			Skin			Lymph		
	PCC $\uparrow$	MSE $\downarrow$	MAE $\downarrow$	PCC $\uparrow$	MSE $\downarrow$	MAE $\downarrow$	PCC $\uparrow$	MSE $\downarrow$	MAE $\downarrow$
STNet	0.0010 $\pm$ 0.0008	0.5682 $\pm$ 0.0270	0.5186 $\pm$ 0.0152	0.0002 $\pm$ 0.0010	0.7161 $\pm$ 0.0508	0.5755 $\pm$ 0.0204	0.0016 $\pm$ 0.0018	0.3035 $\pm$ 0.0099	0.3846 $\pm$ 0.0038
His2ST	0.0916 $\pm$ 0.0550	0.1899 $\pm$ 0.0115	0.2997 $\pm$ 0.0088	0.1197 $\pm$ 0.0574	0.2041 $\pm$ 0.0076	0.3334 $\pm$ 0.0038	0.1480 $\pm$ 0.0441	0.1428 $\pm$ 0.0039	0.2317 $\pm$ 0.0038
BLEEP	0.1057 $\pm$ 0.0521	0.2009 $\pm$ 0.0199	0.2956 $\pm$ 0.0200	0.0696 $\pm$ 0.0284	0.2241 $\pm$ 0.0131	0.3354 $\pm$ 0.0096	0.0622 $\pm$ 0.0249	0.1814 $\pm$ 0.0239	0.2473 $\pm$ 0.0149
MCLSTExp	0.4654 $\pm$ 0.0493	0.1096 $\pm$ 0.0069	0.2162 $\pm$ 0.0065	0.2810 $\pm$ 0.0227	0.1595 $\pm$ 0.0072	0.2888 $\pm$ 0.0055	0.1248 $\pm$ 0.0245	0.1842 $\pm$ 0.0095	0.2515 $\pm$ 0.0083
PEaRL (ours)	<b>0.5868 <math>\pm</math> 0.0359</b>	<b>0.0732 <math>\pm</math> 0.0033</b>	<b>0.1828 <math>\pm</math> 0.0043</b>	<b>0.3756 <math>\pm</math> 0.0148</b>	<b>0.1405 <math>\pm</math> 0.0071</b>	<b>0.2726 <math>\pm</math> 0.0073</b>	<b>0.2352 <math>\pm</math> 0.0145</b>	<b>0.1425 <math>\pm</math> 0.0058</b>	<b>0.2278 <math>\pm</math> 0.0031</b>

Table 2. Performance comparison on **Pathway Expression** prediction across datasets. Results are mean  $\pm$  std. Best per column in **bold**.

Method	Breast			Skin			Lymph		
	PCC $\uparrow$	MSE $\downarrow$	MAE $\downarrow$	PCC $\uparrow$	MSE $\downarrow$	MAE $\downarrow$	PCC $\uparrow$	MSE $\downarrow$	MAE $\downarrow$
STNet	0.0006 $\pm$ 0.0031	0.1469 $\pm$ 0.0037	0.3052 $\pm$ 0.0040	0.0008 $\pm$ 0.0023	0.1972 $\pm$ 0.0040	0.3538 $\pm$ 0.0035	0.0018 $\pm$ 0.0022	0.1197 $\pm$ 0.0191	0.2596 $\pm$ 0.0197
His2ST	0.2008 $\pm$ 0.0270	0.0045 $\pm$ 0.0003	0.0506 $\pm$ 0.0014	0.1071 $\pm$ 0.0501	0.0046 $\pm$ 0.0002	0.0520 $\pm$ 0.0016	0.0324 $\pm$ 0.0280	0.0040 $\pm$ 0.0003	0.0480 $\pm$ 0.0014
BLEEP	0.0560 $\pm$ 0.0714	0.0036 $\pm$ 0.0004	0.0449 $\pm$ 0.0033	0.0958 $\pm$ 0.0703	0.0054 $\pm$ 0.0009	0.0540 $\pm$ 0.0042	0.0610 $\pm$ 0.0317	0.0062 $\pm$ 0.0009	0.0602 $\pm$ 0.0052
MCLSTExp	0.4197 $\pm$ 0.0465	0.0020 $\pm$ 0.0001	0.0333 $\pm$ 0.0010	0.3306 $\pm$ 0.0386	0.0034 $\pm$ 0.0003	0.0430 $\pm$ 0.0015	<b>0.2396 <math>\pm</math> 0.0155</b>	0.0029 $\pm$ 0.0002	0.0405 $\pm$ 0.0016
PEaRL (ours)	<b>0.5055 <math>\pm</math> 0.0271</b>	<b>0.0017 <math>\pm</math> 0.0001</b>	<b>0.0314 <math>\pm</math> 0.0010</b>	<b>0.3523 <math>\pm</math> 0.0336</b>	<b>0.0029 <math>\pm</math> 0.0002</b>	<b>0.0404 <math>\pm</math> 0.0012</b>	0.2247 $\pm$ 0.0353	<b>0.0028 <math>\pm</math> 0.0003</b>	<b>0.0401 <math>\pm</math> 0.0018</b>

**Baselines.** We benchmark PEaRL against several state-of-the-art models for histology–transcriptomics integration. **ST-Net** [11] employs a CNN encoder trained with regression loss to predict spot-level gene expression. **Hist2ST** [51] combines a ConvMixer encoder with a GraphSAGE module and optimizes with regression loss. **BLEEP** [46] adopts a ResNet/ViT encoder trained with a contrastive loss to align image and expression embeddings. **mclSTExp** [29] employs CNN encoders with spatial integer encoding, also trained with a contrastive loss.

**Evaluation metrics.** Model performance on gene and pathway expression prediction is evaluated using Pearson correlation coefficient (PCC), mean squared error (MSE), and mean absolute error (MAE) between predicted and ground-truth values as per previous studies [11, 46, 51]. For survival analysis, we report the concordance index (C-index), which measures the agreement between predicted risk scores and observed survival outcomes [4, 43, 48].

**Implementations.** All models were trained using 5-fold cross-validation. PEaRL was optimized using AdamW with a learning rate of  $1 \times 10^{-4}$ , weight decay of  $1 \times 10^{-3}$ , and trained for up to 100 epochs with early stopping (patience 15). The pathway encoder is a Transformer with two attention layers ( $h = 8$  heads,  $d_k = 64$  dimensions each). Experiments were conducted on one NVIDIA Quadro RTX 8000 GPU.

## 4.2. Quantitative Results

**Gene expression prediction.** As shown in Table 1, across all three datasets, PEaRL consistently improves over baseline methods in terms of PCC. On the breast dataset, PEaRL achieves a PCC of 0.5868 compared to 0.4654 for the strongest baseline (MCLSTExp), corresponding to a 26.1% relative gain. On the skin dataset, PEaRL obtains 0.3756 vs. 0.2810 for MCLSTExp, a 33.7% improvement. The largest margin is observed on the lymph dataset, where PEaRL

reaches 0.2352 compared to 0.1480 for His2ST, yielding a 58.9% relative increase.

**Pathway expression prediction.** For pathway-level targets, PEaRL achieves notable gains on the breast dataset, improving from PCC of 0.4197 (MCLSTExp) to 0.5055, a 20.4% relative increase (see Table 2). On skin, PEaRL improves from PCC of 0.3306 to 0.3523 (6.6%), while on lymph the performance is slightly lower. Overall, the strongest benefit is observed in the breast dataset.

**Survival analysis.** We further evaluated prognostic utility on TCGA-BRCA whole-slide images using an AB-MIL framework [14] trained with a Cox partial likelihood objective. All models were trained and evaluated under a 5-fold cross-validation setting. As shown in Table 3, PEaRL achieved the highest concordance index (C-index =  $0.659 \pm 0.027$ ), surpassing both purely histology-based encoders such as ResNet50 ( $0.513 \pm 0.031$ ) and UNI ( $0.588 \pm 0.046$ ), as well as multimodal baselines such as mclstexp ( $0.612 \pm 0.029$ ), which incorporate only gene-level information. These results demonstrate that multimodal pathway-vision models capture prognostic trends more effectively than embeddings derived from histology alone or from gene-level representations.

Table 3. Survival analysis on **TCGA-BRCA** (C-index). Results are mean  $\pm$  std.

Pretraining Modality	Image Encoders	c-index
ImageNet-1K	ResNet50	$0.513 \pm 0.031$
WSI	UNI	$0.588 \pm 0.046$
WSI+Gene	mclstexp	$0.612 \pm 0.029$
WSI+Pathway	PEaRL	<b><math>0.659 \pm 0.027</math></b>

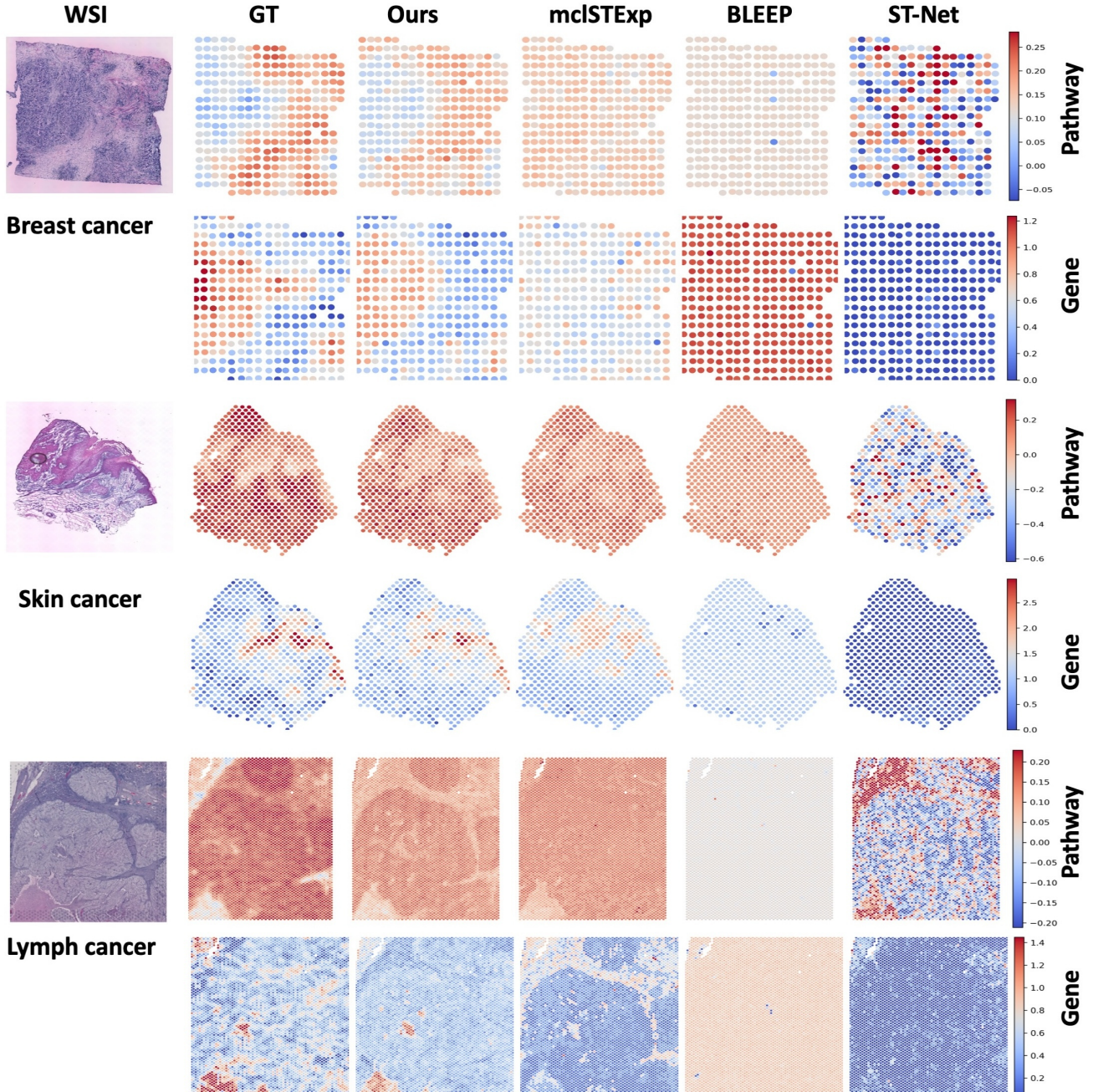


Figure 3. Visualization of expression predictions of different pathways and their corresponding genes across three datasets compared with three baseline methods. We show Hallmark\_allograft\_rejection pathway and its gene HLA-DMB for the breast cancer case; Hallmark\_epithelial\_mesenchymal transition pathway and its gene QSOX1 for the skin cancer case; Reactome\_ABC\_family\_proteins\_mediated\_transport and its gene DERL3 for the lymph carcinoma case.

### 4.3. Ablations

We performed ablation experiments on the breast cancer dataset to disentangle the contributions of different model components and design choices, summarized in Table 4.

**Single-modality encoders.** We here evaluated unimodal

models. Using the image encoder alone allows us to test how much predictive signal can be derived purely from histology, independent of molecular priors. Conversely, using only the pathway encoder to predict gene expression directly evaluates the strength of pathway-derived features. While the pathway-only setup achieves strong performance

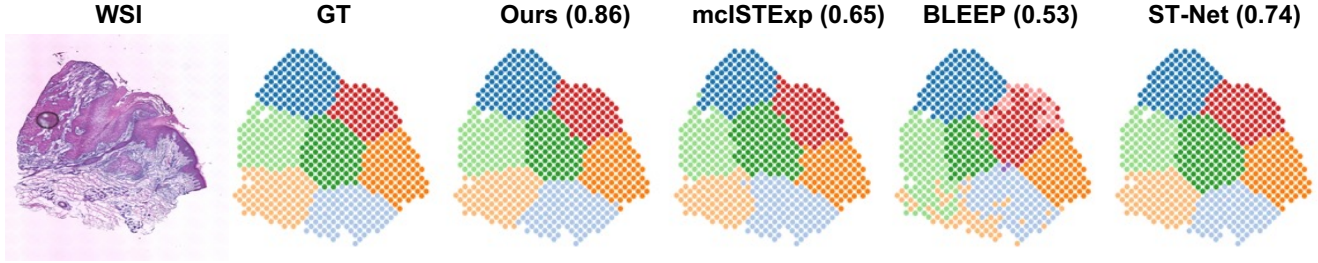


Figure 4. Visualization of the Leiden clusterings for ground truth (GT) and predicted gene expressions (for a skin cancer sample) using PEaRL and other baselines. ARI index shown in (.).

Table 4. Ablation analysis on **Breast** dataset for Gene and Pathway prediction. Results are mean  $\pm$  std.

Breast	Gene Prediction			Pathway Prediction		
	PCC $\uparrow$	MSE $\downarrow$	MAE $\downarrow$	PCC $\uparrow$	MSE $\downarrow$	MAE $\downarrow$
Image encoder (UNI) only	0.1882 $\pm$ 0.014	0.4316 $\pm$ 0.025	0.4760 $\pm$ 0.015	0.1814 $\pm$ 0.010	0.0971 $\pm$ 0.003	0.2513 $\pm$ 0.006
Pathway encoder only	0.2154 $\pm$ 0.016	0.3757 $\pm$ 0.025	0.4125 $\pm$ 0.018	0.4265 $\pm$ 0.026	0.0118 $\pm$ 0.000	0.0880 $\pm$ 0.001
PEaRL (UNI default)	<b>0.5868 <math>\pm</math> 0.0359</b>	<b>0.0732 <math>\pm</math> 0.0033</b>	<b>0.1828 <math>\pm</math> 0.0043</b>	<b>0.5055 <math>\pm</math> 0.0271</b>	<b>0.0017 <math>\pm</math> 0.0001</b>	<b>0.0314 <math>\pm</math> 0.0010</b>
PEaRL w/ ResNet50	0.3729 $\pm$ 0.0511	0.1351 $\pm$ 0.0074	0.2430 $\pm$ 0.0074	0.3337 $\pm$ 0.0500	0.0023 $\pm$ 0.0002	0.0360 $\pm$ 0.0014
PEaRL w/ DenseNet121	0.4833 $\pm$ 0.0634	0.1090 $\pm$ 0.0024	0.2180 $\pm$ 0.0019	0.3822 $\pm$ 0.0549	0.0022 $\pm$ 0.0002	0.0349 $\pm$ 0.0014
PEaRL w/ ViT-B	0.3573 $\pm$ 0.0389	0.1380 $\pm$ 0.0056	0.2459 $\pm$ 0.0062	0.3303 $\pm$ 0.0344	0.0023 $\pm$ 0.0001	0.0356 $\pm$ 0.0006

on pathway prediction by construction, it is also more effective than the image encoder for gene expression prediction (PCC = 0.2154 vs. 0.1882). This indicates that while histology carries complementary information, pathway-level features are inherently more predictive. This highlights the critical role of incorporating pathway priors beyond morphology alone.

**Different image encoders.** Next, we examined the impact of varying the architecture of the image encoder (Table 4). We compared three types of models: (i) conventional CNNs such as ResNet50 and DenseNet121, (ii) a Vision Transformer (ViT), and (iii) UNI, a foundation model pretrained on large-scale histopathology images. Note that apart from UNI, all three encoders were trained from scratch with our PEaRL framework. Across both *gene expression* and *pathway prediction* tasks, UNI consistently achieved the best performance, showcasing the advantage of pretraining on domain-specific histopathology corpora. CNNs and ViTs, while competitive, lagged behind UNI, demonstrating that generic backbones are less effective.

#### 4.4. Qualitative Results

**Breast cancer pathway and gene visualization.** Fig. 3 shows visualizations of the Hallmark allograft rejection pathway [22, 26] and the corresponding HLA-DMB gene in the breast cancer dataset. This pathway captures immune-related activity, which is highly relevant in breast tumor microenvironments. The HLA-DMB gene is an important component of the antigen presentation machinery and plays

a role in immune surveillance. Our pathway maps reveal spatially distinct immune activity within the tissue, which is reflected consistently in the gene-level predictions. Together, the pathway- and gene-level visualizations demonstrate that PEaRL can capture not only global immune signaling but also its spot-level variation, producing coherent and biologically meaningful maps compared to SOTA. Additional heatmaps can be seen in supplementary Fig. 9-10.

**Leiden clustering analysis.** We use Leiden clustering, a graph-based community detection algorithm, to partition spots into coherent groups [3, 40]. By clustering the predicted expression maps, we assess whether the model reconstructs biologically meaningful tissue structures. To evaluate cluster agreement, we use the Adjusted Rand Index (ARI), which measures similarity between predicted and ground-truth clusters while correcting for random chance. PEaRL achieves higher ARI scores than baselines (Fig. 4). Leiden clustering of the breast and lymph cancer samples are shown in supplementary Figs. 7-8. We also show correlation plots for three datasets in the supplementary Figs. 5-6.

## 5. Conclusion

In this work, we introduced PEaRL, a novel multimodal framework that integrates histology images with pathway-informed transcriptomic representations to predict gene and pathway expression from histology images. Our experiments across multiple cancer ST datasets demonstrate that PEaRL consistently outperforms existing baselines in both

gene and pathway prediction tasks, and in the capture of prognostic information. Furthermore, qualitative analyses revealed that PEaRL recovers biologically meaningful spatial patterns, maintains co-expression structure, and produces clusters that align with histological regions. Together, these results highlight PEaRL’s ability to bridge the gap between molecular and morphological views of cancer. Future work will extend this framework to pan-cancer datasets, incorporate additional modalities, and explore clinical applications such as biomarker discovery and treatment response prediction.

**Acknowledgements.** This research was partially supported by National Institutes of Health (NIH) and National Cancer Institute (NCI) grants 1R21CA258493-01A1, 1R01CA297843-01, 3R21CA258493-02S1, 1R03DE033489-01A1, and National Science Foundation (NSF) grant 2442053. The content is solely the responsibility of the authors and does not necessarily represent the official views of the National Institutes of Health.

## References

- [1] Luca Abatangelo, Rosalia Maglietta, Angela Distaso, Annarita D’Addabbo, Teresa Maria Creanza, Sayan Mukherjee, and Nicola Ancona. Comparative study of gene set enrichment methods. *BMC bioinformatics*, 10:1–12, 2009. 3, 5
- [2] Alma Andersson, Ludvig Larsson, Linnea Stenbeck, Fredrik Salmén, Anna Ehinger, Sunny Z Wu, Ghamdan Al-Eryani, Daniel Roden, Alex Swarbrick, Åke Borg, et al. Spatial deconvolution of her2-positive breast cancer delineates tumor-associated cell type interactions. *Nature communications*, 12(1):6012, 2021. 2, 5
- [3] Siti Haryanti Hairol Anuar, Zuraida Abal Abas, Norhazwani Mohd Yunos, Nurul Hafizah Mohd Zaki, Nurul Akmal Hashim, Mohd Fariddudin Mokhtar, Siti Azirah Asmai, Zaheera Zainal Abidin, and Ahmad Fadzli Nizam. Comparison between louvain and leiden algorithm for network structure: a review. In *Journal of Physics: Conference Series*, page 012028. IOP Publishing, 2021. 8
- [4] Richard J Chen, Ming Y Lu, Wei-Hung Weng, Tiffany Y Chen, Drew FK Williamson, Trevor Manz, Maha Shady, and Faisal Mahmood. Multimodal co-attention transformer for survival prediction in gigapixel whole slide images. In *Proceedings of the IEEE/CVF international conference on computer vision*, pages 4015–4025, 2021. 6
- [5] Richard J Chen, Ming Y Lu, Wei-Hung Weng, Tiffany Y Chen, Drew FK Williamson, Trevor Manz, Maha Shady, and Faisal Mahmood. Multimodal co-attention transformer for survival prediction in gigapixel whole slide images. In *Proceedings of the IEEE/CVF international conference on computer vision*, pages 4015–4025, 2021. 1, 3
- [6] Richard J Chen, Chengkuan Chen, Yicong Li, Tiffany Y Chen, Andrew D Trister, Rahul G Krishnan, and Faisal Mahmood. Scaling vision transformers to gigapixel images via hierarchical self-supervised learning. In *Proceedings of the IEEE/CVF conference on computer vision and pattern recognition*, pages 16144–16155, 2022. 3
- [7] Richard J Chen, Tong Ding, Ming Y Lu, Drew FK Williamson, Guillaume Jaume, Bowen Chen, Andrew Zhang, Daniel Shao, Andrew H Song, Muhammad Shaban, et al. A general-purpose self-supervised model for computational pathology. *arXiv preprint arXiv:2308.15474*, 2023. 3, 5
- [8] Antonio Fabregat, Steven Jupe, Lisa Matthews, Konstantinos Sidiropoulos, Marc Gillespie, Phani Garapati, Robin Haw, Bijay Jassal, Florian Korninger, Bruce May, et al. The reactome pathway knowledgebase. *Nucleic acids research*, 46(D1):D649–D655, 2018. 5
- [9] Simon Graham, Quoc Dang Vu, Shan E Ahmed Raza, Ayesha Azam, Yee Wah Tsang, Jin Tae Kwak, and Nasir Rajpoot. Hover-net: Simultaneous segmentation and classification of nuclei in multi-tissue histology images. *Medical image analysis*, 58:101563, 2019. 1
- [10] Bryan He, Ludvig Bergensträhle, Linnea Stenbeck, Abubakar Abid, Alma Andersson, Åke Borg, Jonas Maaskola, Joakim Lundeberg, and James Zou. Integrating spatial gene expression and breast tumour morphology via deep learning. *Nature biomedical engineering*, 4(8): 827–834, 2020. 2, 3
- [11] Bryan He, Ludvig Bergensträhle, Linnea Stenbeck, Abubakar Abid, Alma Andersson, Åke Borg, Jonas Maaskola, Joakim Lundeberg, and James Zou. Integrating spatial gene expression and breast tumour morphology via deep learning. *Nature biomedical engineering*, 4(8): 827–834, 2020. 6
- [12] Fabian Hörst, Moritz Rempe, Lukas Heine, Constantin Seibold, Julius Keyl, Giulia Baldini, Selma Ugurel, Jens Siveke, Barbara Grünwald, Jan Egger, et al. Cellvit: Vision transformers for precise cell segmentation and classification. *Medical Image Analysis*, 94:103143, 2024. 1
- [13] Zhi Huang, Federico Bianchi, Mert Yuksekogonul, Thomas J Montine, and James Zou. A visual–language foundation model for pathology image analysis using medical twitter. *Nature medicine*, 29(9):2307–2316, 2023. 3
- [14] Maximilian Ilse, Jakub Tomczak, and Max Welling. Attention-based deep multiple instance learning. In *International conference on machine learning*, pages 2127–2136. PMLR, 2018. 6
- [15] Guillaume Jaume, Anurag Vaidya, Richard J Chen, Drew FK Williamson, Paul Pu Liang, and Faisal Mahmood. Modeling dense multimodal interactions between biological pathways and histology for survival prediction. In *Proceedings of the IEEE/CVF Conference on Computer Vision and Pattern Recognition*, pages 11579–11590, 2024. 3
- [16] Guillaume Jaume, Anurag Vaidya, Richard J Chen, Drew FK Williamson, Paul Pu Liang, and Faisal Mahmood. Modeling dense multimodal interactions between biological pathways and histology for survival prediction. In *Proceedings of the IEEE/CVF Conference on Computer Vision and Pattern Recognition*, pages 11579–11590, 2024. 1
- [17] Guillaume Jaume, Paul Doucet, Andrew Song, Ming Yang Lu, Cristina Almagro Pérez, Sophia Wagner, Anurag Vaidya, Richard Chen, Drew Williamson, Ahnong Kim, et al. Hest-1k: A dataset for spatial transcriptomics and histology image

- analysis. *Advances in Neural Information Processing Systems*, 37:53798–53833, 2025. 5
- [18] Andrew L Ji, Adam J Rubin, Kim Thrane, Sizun Jiang, David L Reynolds, Robin M Meyers, Margaret G Guo, Benson M George, Annelie Mollbrink, Joseph Bergenstr hle, et al. Multimodal analysis of composition and spatial architecture in human squamous cell carcinoma. *cell*, 182(2):497–514, 2020. 2, 5
- [19] Yuran Jia, Junliang Liu, Li Chen, Tianyi Zhao, and Yadong Wang. Thitogene: a deep learning method for predicting spatial transcriptomics from histological images. *Briefings in Bioinformatics*, 25(1):bbad464, 2024. 2, 3
- [20] Osamu Kimura, Yasuteru Kondo, and Tooru Shimosegawa. Ppar could contribute to the pathogenesis of hepatocellular carcinoma. *PPAR research*, 2012(1):574180, 2012. 3
- [21] Brent M Kuenzi and Trey Ideker. A census of pathway maps in cancer systems biology. *Nature Reviews Cancer*, 20(4):233–246, 2020. 3
- [22] Alain Le Moine, Michel Goldman, and Daniel Abramowicz. Multiple pathways to allograft rejection. *Transplantation*, 73(9):1373–1381, 2002. 8
- [23] Arthur Liberzon, Aravind Subramanian, Reid Pinchback, Helga Thorvaldsd ttir, Pablo Tamayo, and Jill P Mesirov. Molecular signatures database (msigdb) 3.0. *Bioinformatics*, 27(12):1739–1740, 2011. 5
- [24] Ming Y Lu, Bowen Chen, Drew F K Williamson, Richard J Chen, Ivy Liang, Tong Ding, Guillaume Jaume, Igor Odintsov, Long Phi Le, Georg Gerber, Anil V Parwani, Andrew Zhang, and Faisal Mahmood. A visual-language foundation model for computational pathology. *Nat. Med.*, 30(3):863–874, 2024. 3
- [25] Teng Ma, Haochen Zhao, Qichang Zhao, and Jianxin Wang. Cox-path: Biological pathway-informed graph neural network for cancer survival prediction. In *Proceedings of the 15th ACM International Conference on Bioinformatics, Computational Biology and Health Informatics*, pages 1–6, 2024. 3
- [26] Jose Marino, Joshua Paster, and Gilles Benichou. Allorecognition by t lymphocytes and allograft rejection. *Frontiers in immunology*, 7:582, 2016. 8
- [27] Maxime Meylan, Florent Petitprez, Etienne Becht, Antoine Bougou in, Guilhem Pupier, Anne Calvez, Ilenia Giglioli, Virginie Verkarre, Guillaume Lacroix, Johanna Verneau, et al. Tertiary lymphoid structures generate and propagate anti-tumor antibody-producing plasma cells in renal cell cancer. *Immunity*, 55(3):527–541, 2022. 2, 5
- [28] Weiming Mi, Junjie Li, Yucheng Guo, Xinyu Ren, Zhiyong Liang, Tao Zhang, and Hao Zou. Deep learning-based multi-class classification of breast digital pathology images. *Cancer Management and Research*, pages 4605–4617, 2021. 1
- [29] Wenwen Min, Zhiceng Shi, Jun Zhang, Jun Wan, and Changmiao Wang. Multimodal contrastive learning for spatial gene expression prediction using histology images. *Briefings in Bioinformatics*, 25(6):bbae551, 2024. 2, 3, 6
- [30] Ali Mortazavi, Brian A Williams, Kenneth McCue, Lorian Schaeffer, and Barbara Wold. Mapping and quantifying mammalian transcriptomes by rna-seq. *Nature methods*, 5(7):621–628, 2008. 1
- [31] M Pang, K Su, and M Li. Leveraging information in spatial transcriptomics to predict super-resolution gene expression from histology images in tumors. *bioRxiv*. 2021; 2021–11. [doi.org/10.1101/2021.11.28](https://doi.org/10.1101/2021.11.28), 2021. 2, 3
- [32] Alec Radford, Jong Wook Kim, Christopher Hallacy, Aditya Ramesh, Gabriel Goh, Sandhini Agarwal, Girish Sastry, Amanda Askell, Pamela Mishkin, Jack Clark, et al. Learning transferable visual models from natural language supervision. In *International Conference on Machine Learning*, pages 8748–8763. PMLR, 2021. 3
- [33] U Raghavendra, U Rajendra Acharya, and Hojjat Adeli. Artificial intelligence techniques for automated diagnosis of neurological disorders. *European neurology*, 82(1-3):41–64, 2020. 1
- [34] Anjali Rao, Dalia Barkley, Gustavo S Fran a, and Itai Yanai. Exploring tissue architecture using spatial transcriptomics. *Nature*, 596(7871):211–220, 2021. 1
- [35] Patrik L St hl, Fredrik Salm n, Sanja Vickovic, Anna Lundmark, Jos  Fern ndez Navarro, Jens Magnusson, Stefania Giacomello, Michaela Asp, Jakub O Westholm, Mikael Huss, et al. Visualization and analysis of gene expression in tissue sections by spatial transcriptomics. *Science*, 353(6294):78–82, 2016. 1
- [36] Aravind Subramanian, Pablo Tamayo, Vamsi K Mootha, Sayan Mukherjee, Benjamin L Ebert, Michael A Gillette, Amanda Paulovich, Scott L Pomeroy, Todd R Golub, Eric S Lander, et al. Gene set enrichment analysis: a knowledge-based approach for interpreting genome-wide expression profiles. *Proceedings of the National Academy of Sciences*, 102(43):15545–15550, 2005. 3
- [37] PJ Sudharshan, Caroline Petitjean, Fabio Spanhol, Luiz Eduardo Oliveira, Laurent Heutte, and Paul Honeine. Multiple instance learning for histopathological breast cancer image classification. *Expert Systems with Applications*, 117:103–111, 2019. 3
- [38] Valentine Svensson, Roser Vento-Tormo, and Sarah A Teichmann. Exponential scaling of single-cell rna-seq in the last decade. *Nature protocols*, 13(4):599–604, 2018. 1
- [39] Fuchou Tang, Catalin Barbacioru, Yangzhou Wang, Ellen Nordman, Clarence Lee, Nanlan Xu, Xiaohui Wang, John Bodeau, Brian B Tuch, Asim Siddiqui, et al. mrna-seq whole-transcriptome analysis of a single cell. *Nature methods*, 6(5):377–382, 2009. 1
- [40] Vincent A Traag, Ludo Waltman, and Nees Jan Van Eck. From louvain to leiden: guaranteeing well-connected communities. *Scientific reports*, 9(1):1–12, 2019. 8
- [41] Quoc Dang Vu, Simon Graham, Tahsin Kurc, Minh Nguyen Nhat To, Muhammad Shaban, Talha Qaiser, Navid Alemi Koohbanani, Syed Ali Khurram, Jayashree Kalpathy-Cramer, Tianhao Zhao, et al. Methods for segmentation and classification of digital microscopy tissue images. *Frontiers in bioengineering and biotechnology*, 7:53, 2019. 1
- [42] Xiyue Wang, Sen Yang, Jun Zhang, Minghui Wang, Jing Zhang, Wei Yang, Junzhou Huang, and Xiao Han. Transformer-based unsupervised contrastive learning for histopathological image classification. *Medical image analysis*, 81:102559, 2022. 3

- [43] Zhong Wang, Mark Gerstein, and Michael Snyder. Rna-seq: a revolutionary tool for transcriptomics. *Nature reviews genetics*, 10(1):57–63, 2009. 6
- [44] F Alexander Wolf, Philipp Angerer, and Fabian J Theis. Scanpy: large-scale single-cell gene expression data analysis. *Genome biology*, 19(1):15, 2018. 5
- [45] Ellery Wulczyn, David F Steiner, Zhaoyang Xu, Apaar Sathwani, Hongwu Wang, Isabelle Flament-Auvigne, Craig H Mermel, Po-Hsuan Cameron Chen, Yun Liu, and Martin C Stumpe. Deep learning-based survival prediction for multiple cancer types using histopathology images. *PloS one*, 15(6):e0233678, 2020. 1, 3
- [46] Ronald Xie, Kuan Pang, Sai Chung, Catia Perciani, Sonya MacParland, Bo Wang, and Gary Bader. Spatially resolved gene expression prediction from histology images via bimodal contrastive learning. *Advances in Neural Information Processing Systems*, 36:70626–70637, 2023. 2, 3, 6
- [47] Hanwen Xu, Naoto Usuyama, Jaspreet Bagga, Sheng Zhang, Rajesh Rao, Tristan Naumann, Cliff Wong, Zelalem Gero, Javier González, Yu Gu, Yanbo Xu, Mu Wei, Wenhui Wang, Shuming Ma, Furu Wei, Jianwei Yang, Chunyuan Li, Jianfeng Gao, Jaylen Rosemon, Tucker Bower, Soohee Lee, Roshanthi Weerasinghe, Bill J Wright, Ari Robicsek, Brian Piening, Carlo Bifulco, Sheng Wang, and Hoifung Poon. A whole-slide foundation model for digital pathology from real-world data. *Nature*, 630(8015):181–188, 2024. 3
- [48] Yingxue Xu and Hao Chen. Multimodal optimal transport-based co-attention transformer with global structure consistency for survival prediction. In *Proceedings of the IEEE/CVF international conference on computer vision*, pages 21241–21251, 2023. 6
- [49] Yan Xu, Jun-Yan Zhu, Eric Chang, and Zhuowen Tu. Multiple clustered instance learning for histopathology cancer image classification, segmentation and clustering. In *2012 IEEE Conference on Computer Vision and Pattern Recognition*, pages 964–971. IEEE, 2012. 3
- [50] Yuansong Zeng, Zhuoyi Wei, Weijiang Yu, Rui Yin, Yuchen Yuan, Bingling Li, Zhonghui Tang, Yutong Lu, and Yuedong Yang. Spatial transcriptomics prediction from histology jointly through transformer and graph neural networks. *Brief. Bioinform.*, 23(5), 2022. 2, 3
- [51] Yuansong Zeng, Zhuoyi Wei, Weijiang Yu, Rui Yin, Yuchen Yuan, Bingling Li, Zhonghui Tang, Yutong Lu, and Yuedong Yang. Spatial transcriptomics prediction from histology jointly through transformer and graph neural networks. *Briefings in Bioinformatics*, 23(5), 2022. 6
- [52] Yilan Zhang, Yingxue Xu, Jianqi Chen, Fengying Xie, and Hao Chen. Prototypical information bottlenecking and disentangling for multimodal cancer survival prediction. *arXiv preprint arXiv:2401.01646*, 2024. 3

## **6. Supplementary Material**

In the supplementary material we begin with the correlation plots (Figures 5 and 6), and show the leiden clusters for the breast and lymph cancer samples (Figures 7 and 8). Finally, we also show additional pathway and gene heatmaps for the breast, skin, and lymph cancer samples (Figures 9 and 10).

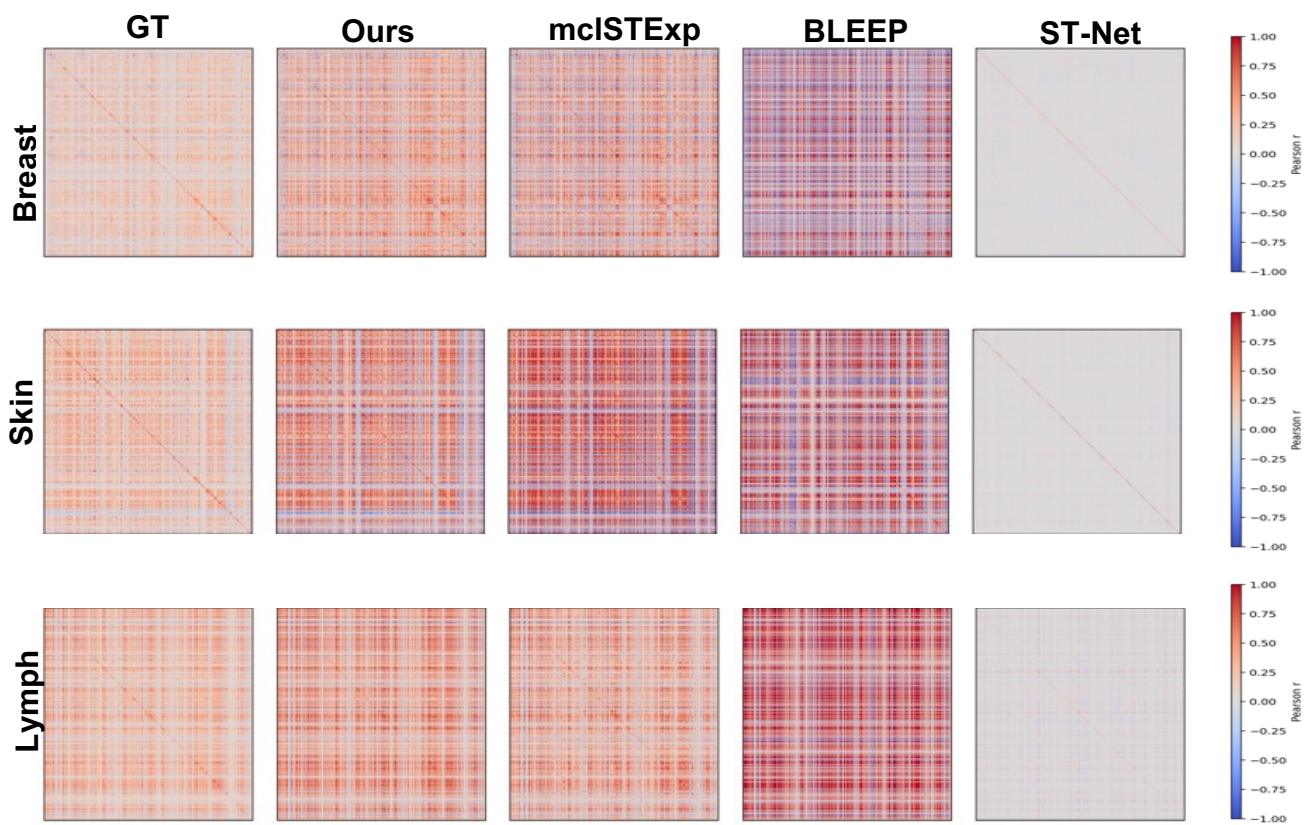


Figure 5. Visualization of the pathway-pathway correlation plots across the three datasets and comparison of PEaRL with baseline models

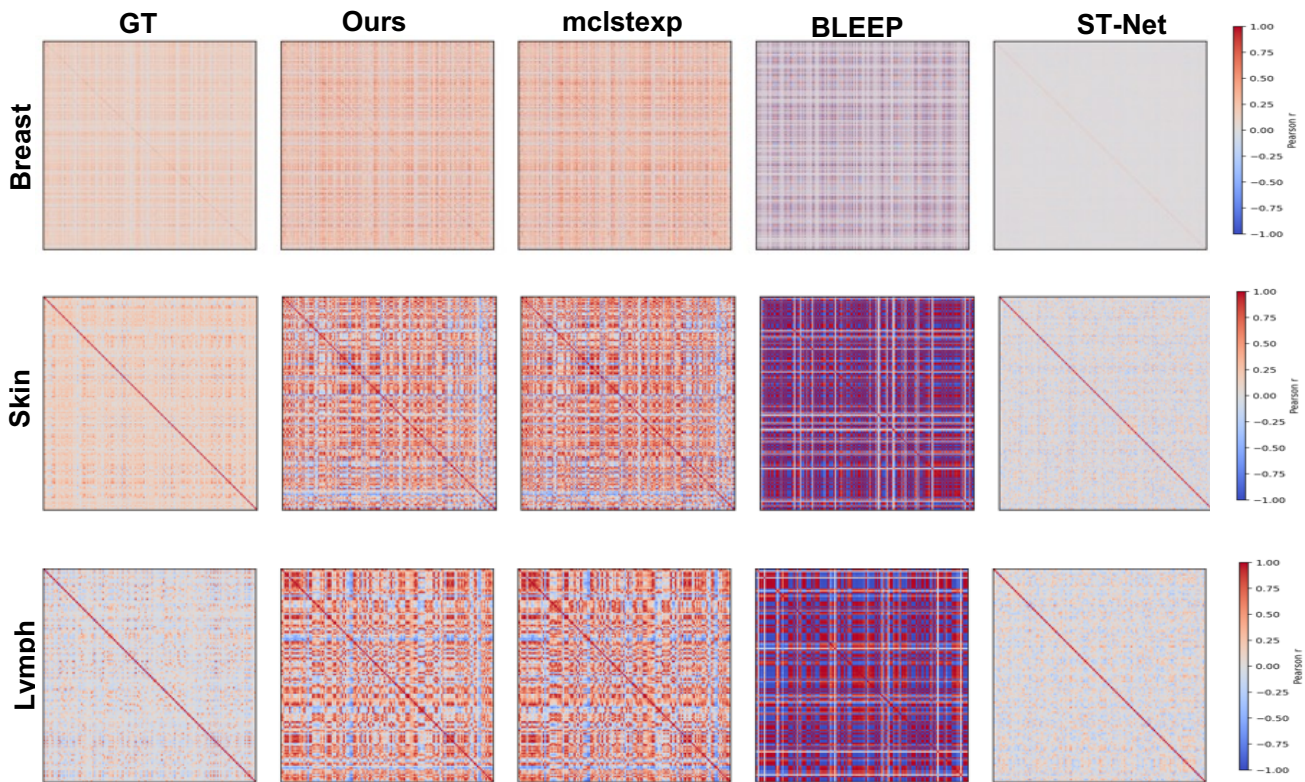


Figure 6. Visualization of the gene-gene correlation plots across the three datasets and comparison of PEaRL with baseline models

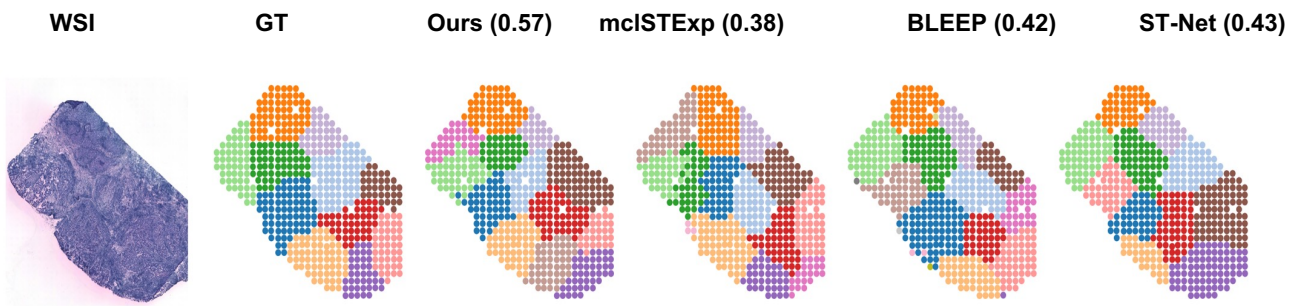


Figure 7. Visualization of Leiden clusterings for ground truth and predicted gene expressions for the breast cancer dataset. ARI index shown in (.)

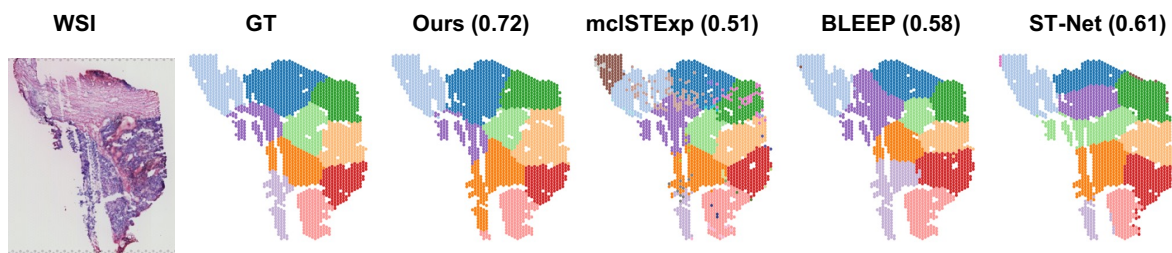


Figure 8. Visualization of Leiden clusterings for ground truth and predicted gene expressions for the lymph cancer sample. ARI index shown in (.)

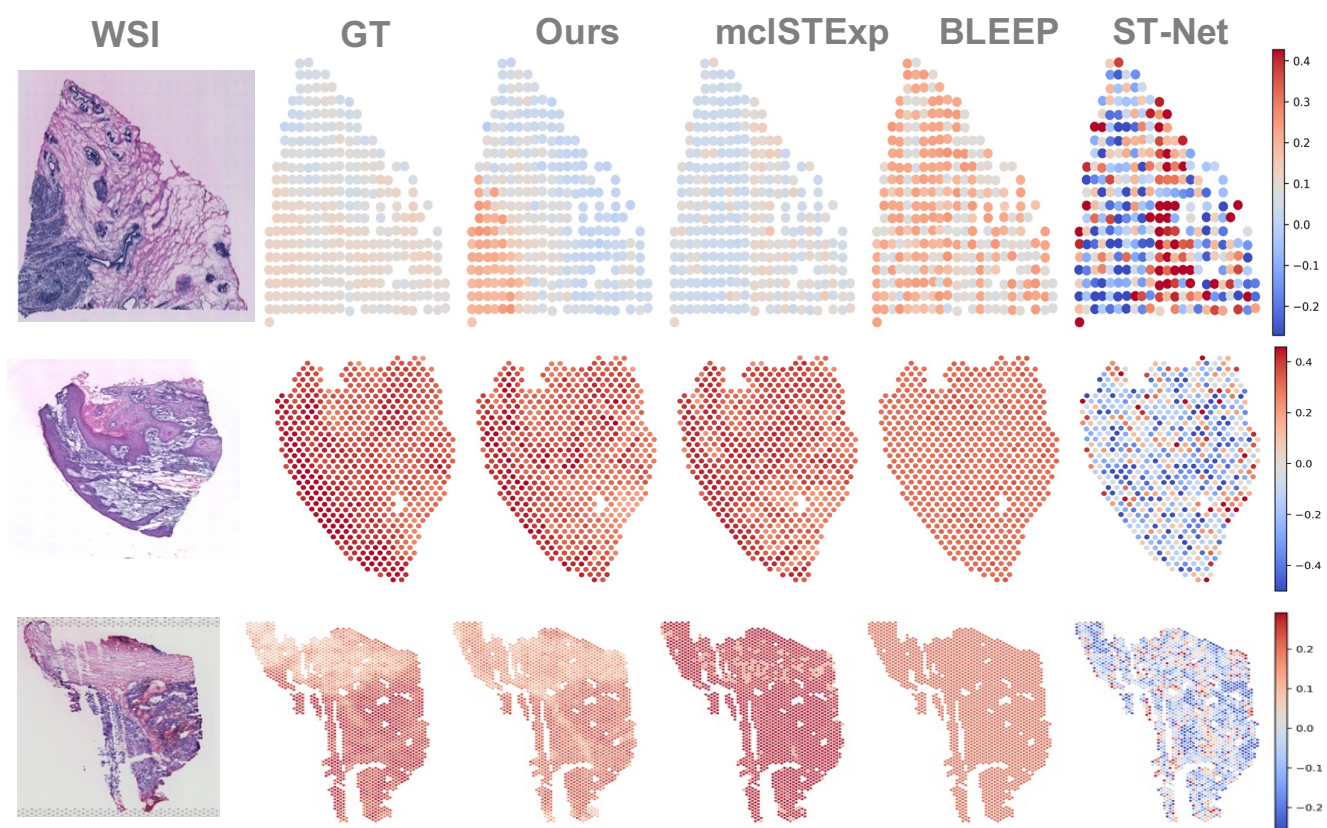


Figure 9. Visualization of pathway heatmaps across the three datasets. We show the `Hallmark_Myc_targets_v1` pathway for the breast sample, `Reactome_Eukaryotic_Translation_Initiation` for the skin sample, and `Reactome_ABC_family_of_proteins_mediated_transport` for the lymph cancer sample.

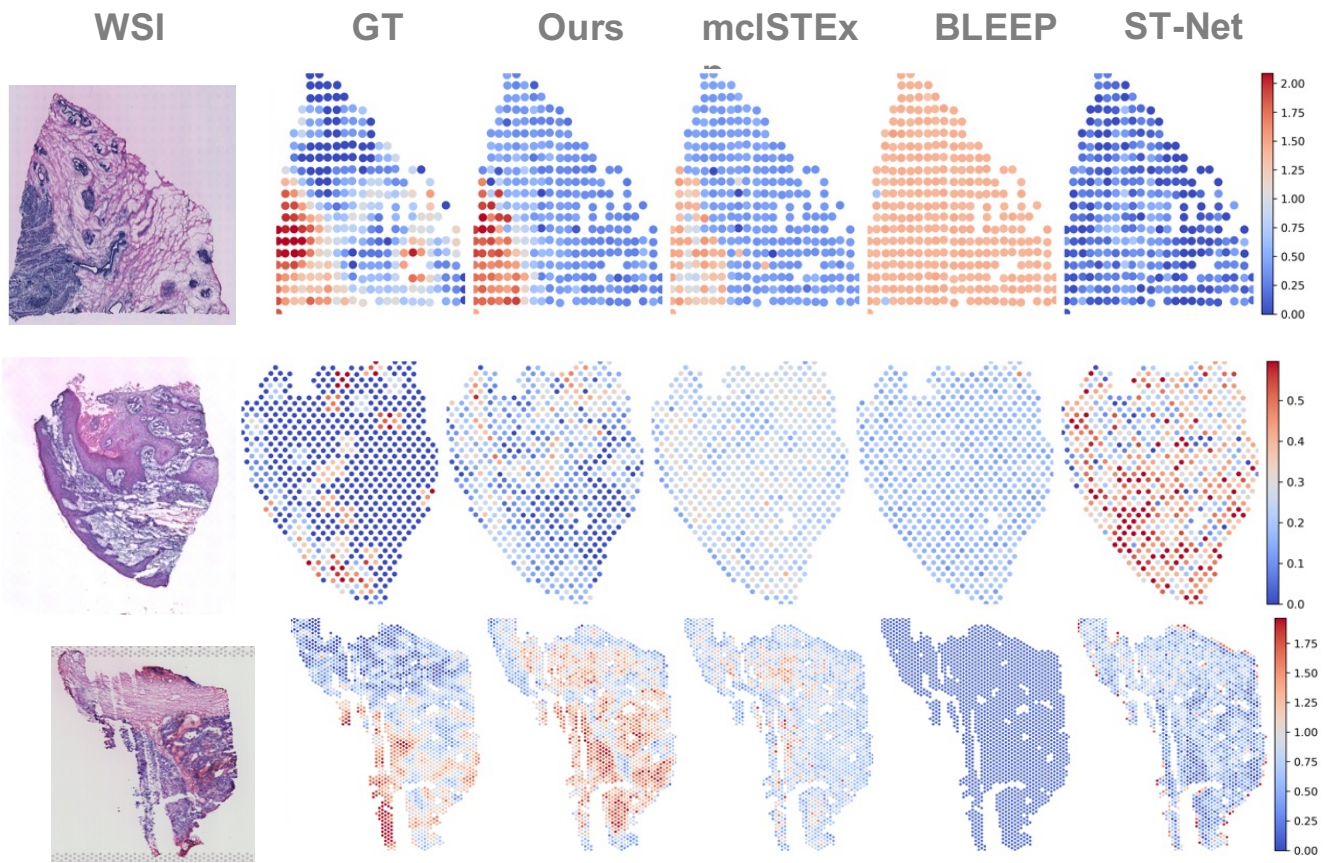


Figure 10. Visualization of the gene heatmaps across the three datasets. We show genes SSBP1, E1F4EBP1, and PKP2 for the breast, skin, and the lymph cancer samples respectively.